

Granular topological insulators

Abhishek Banerjee¹, Oindrila Deb², Kunjalata Majhi¹,

R. Ganesan¹, Diptiman Sen², and P. S. Anil Kumar^{1,3}

¹*Department of Physics, Indian Institute of Science, Bengaluru 560 012, India*

²*Centre for High Energy Physics, Indian Institute of Science, Bengaluru 560 012, India*

³ *Centre for Nano Science and Engineering,
Indian Institute of Science, Bengaluru 560 012, India*

(Dated: August 19, 2018)

Abstract

Granular conductors form an artificially engineered class of solid state materials wherein the microstructure can be tuned to mimic a wide range of otherwise inaccessible physical systems. At the same time, topological insulators (TIs) have become a cornerstone of modern condensed matter physics as materials hosting metallic states on the surface and insulating in the bulk. However it remains to be understood how granularity affects this new and exotic phase of matter. We perform electrical transport experiments on highly granular topological insulator thin films of Bi₂Se₃ and reveal remarkable properties. We observe clear signatures of topological surface states despite granularity with distinctly different properties from conventional bulk TI systems including sharp surface state coupling-decoupling transitions, large surface state penetration depths and exotic Berry phase effects. We present a model which explains these results. Our findings illustrate that granularity can be used to engineer designer TIs, at the same time allowing easy access to the Dirac-fermion physics that is inaccessible in single crystal systems.

In solid state systems, granularity can be conceptually introduced by considering nanoscale sized grains that are packed to form a macroscopic system. While the constituent granules are large enough to retain the characteristic properties of the parent material, they are also subject to strong quantum confinement. Depending on how the granules couple to their neighbours, a host of physical systems can be realized [1–3]. Granular media have therefore been used as a test bed for studying a rich variety of physical phenomena including metal-insulator transitions [4, 5], superconductivity [6] and magnetism [7], apart from a versatile range of applications including solar cells, light emitting diodes, photodetectors and field-effect transistors [8–10].

The extension of these ideas to the case of three-dimensional topological insulators (TIs) however remains unknown. In the recent surge of interest in this novel phase of matter [11, 12], a lot of experimental [13–19] and theoretical [20–26] activity has been directed at understanding their physical properties, the most interesting of which is the presence of gapless Dirac fermions on the surfaces of these materials. The chiral nature of these surface fermions follows from the strong spin-orbit coupling and ensures that the momentum of an electron fixes the direction of its spin. The situation is however not so simple when one deviates from an ideal TI. For example, it has been shown that bulk disorder may completely randomize the surface spin polarization [27]. Also, strong bulk-to-surface coupling in bulk-doped TIs may delocalize surface states [28]. It is not clear whether such surface states can manifest in highly granular TIs. This motivates us to ask the following questions: (i) how does granularity affect TIs, and (ii) can granularity be used to tune the properties of TIs? We will concentrate on the specific case of 3D TIs in this work.

Granular Bi_2Se_3 thin films are grown on high resistivity Si(111) substrates using pulsed laser deposition. The degree of granularity is controlled by tuning the laser pulse energy and is quantified using x-ray diffraction and atomic force microscopy (see Supplementary Information for details). Our measurements indicate an in-plane coherence length $\xi_{\parallel} \approx 10$ nm, which is the same as the in-plane grain size. The vertical grain size is smaller and is estimated to be $\sim 2\text{--}3$ nm. Our thin films are therefore composed of highly ordered aggregates of granules and can be schematically depicted as shown in Fig. 1 (a). Although the granular packing is largely uniform, we expect an asymmetry in the inter-granular coupling. While the in-plane coupling is expected to be strong due to a large density of lateral dangling bonds, the absence of dangling bonds in the vertical directions makes the vertical inter-grain

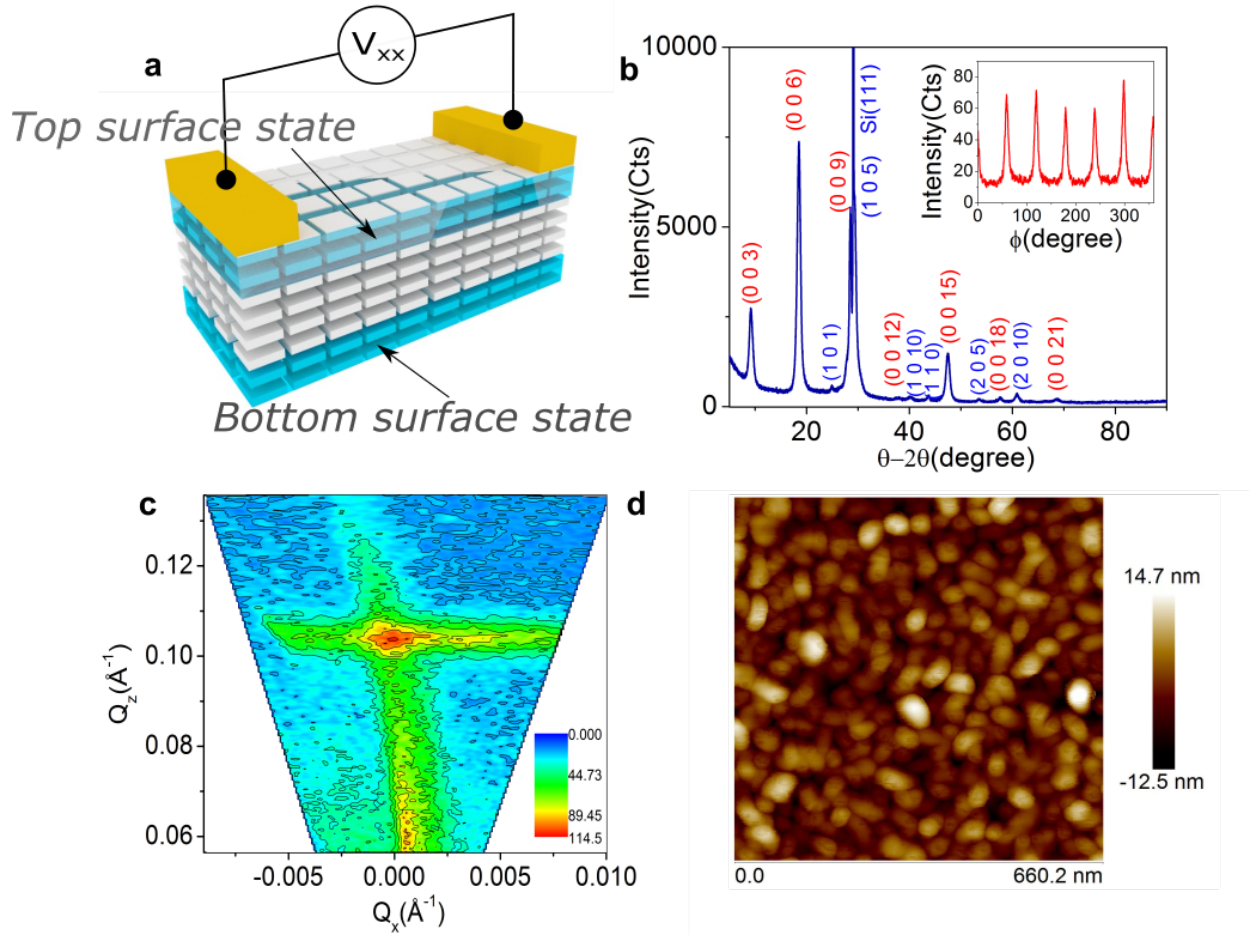


FIG. 1. **Growth of granular TI thin films** (a) Schematic of a granular conductor composed of ordered TI granules. Under appropriate conditions, the entire conductor behaves as a single crystal TI with distinct top and bottom surface states. The finite penetration depth of the surface states is shown in blue. (b) Standard $\theta - 2\theta$ XRD scan of a typical granular thin film shows that (003n) peaks (marked in red) are dominant implying a preferential orientation in the c -axis direction. Non-oriented peaks (marked in blue) reflect the granularity of our samples. Inset: Azimuthal scan of (105) planes of Bi_2Se_3 shows six-fold symmetry and a large FWHM $\sim 8^\circ$. (c) Reciprocal space maps of (003) peak indicate highly granular thin films. The large broadening of the reciprocal lattice peak is indicative of a highly granular material, with grain sizes that roughly scale as the inverse of the peak broadening. (d) AFM image showing the surface topography of a granular sample.

coupling weak.

Electronic transport measurements are carried out on granular TI films with thickness

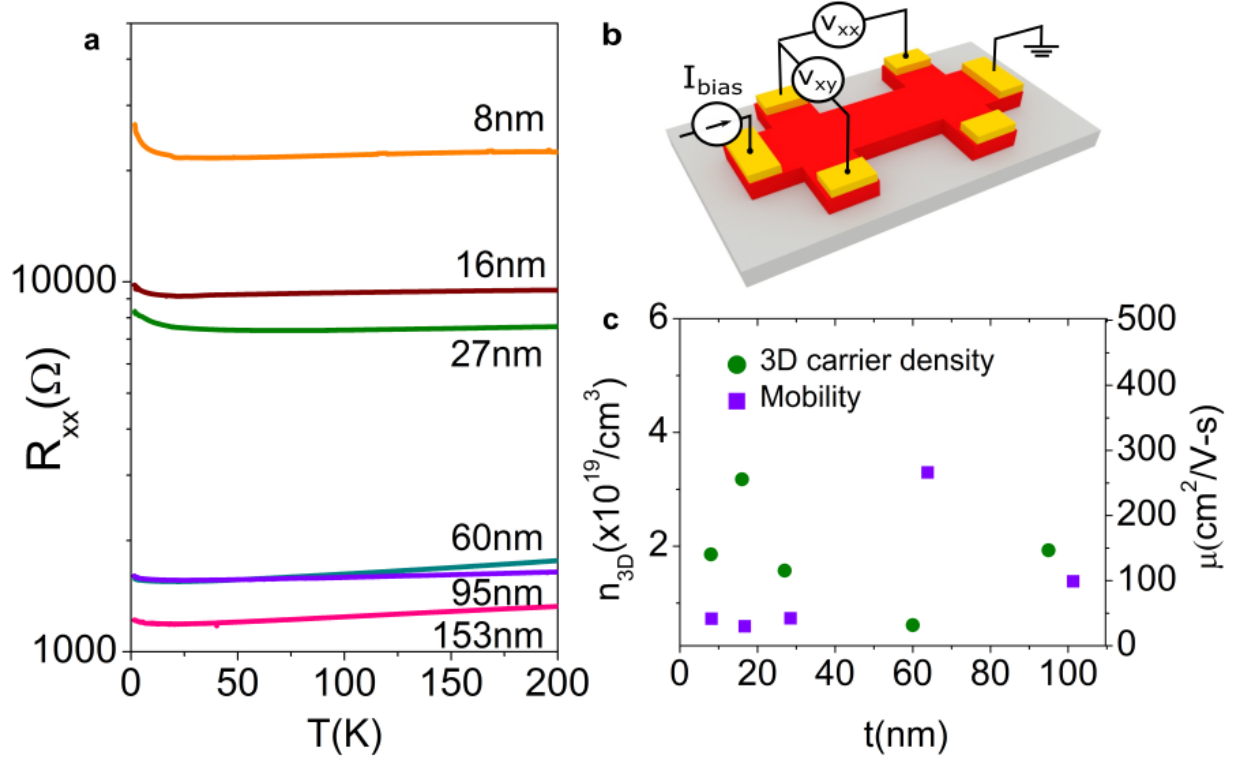


FIG. 2. **Hall conductivity and resistivity of granular TI conductors** (a) Resistance versus temperature curves for granular samples with different thicknesses. (b) Schematic of the six probe Hall bar configuration that is used to measure the longitudinal and transverse resistance independently. (c) Hall carrier density and mobility for different sample thicknesses at $T = 2$ K.

ranging from 8 nm to 153 nm. The resistance versus temperature curves for granular TI samples shown in Fig. 2 (a) suggest weakly metallic conductivity for all samples. At low temperatures a strong insulating upturn is seen below ~ 30 K. Both the resistance minimum and the onset of the upturn are enhanced for films with lower thickness. This is a result of inter-grain hopping (discussed later) of electrons that is the dominant transport mechanism at low temperatures [1]. At higher temperatures, however, the conductance is determined instead by the intra-grain conductance that is limited by long-range impurity scattering from charged defect centres. A striking feature of our data is that for films with higher thickness (60 nm - 153 nm), the conductance does not vary much with the sample thickness. This is

indicative of surface confined transport in the thick film regime where the top and bottom surface states do not overlap. This is surprising given that the multiply connected geometry of our thin films is naively not expected to give rise to well-defined surface excitations.

Hall effect measurements (at 2 K) are used to estimate the disorder introduced by granularity. The values of carrier density (n_{3D}) and mobility (μ) are shown in Fig. 2 (c). For a typical sample, assuming a spherical Fermi surface we estimate a Fermi momentum $k_F = (3\pi^2 n_{3D})^{1/3} \sim 0.8 - 0.9 \text{ nm}^{-1}$ and a mean free path $l_e = (\hbar\mu/e)k_F \sim 2 - 3 \text{ nm}$. The extent of disorder in our samples can be estimated by using the Ioffe-Regel criterion for which $k_F l_e \gg 1$ implies weakly disordered conduction while $k_F l_e \ll 1$ implies strong localization. For our samples, $k_F l_e \sim 2 - 3$ which puts our samples in a regime proximate to the localization transition. The small grain size limits the mean free path of electrons. While intra-grain transport remains diffusive, the proximity to localization is a consequence of limited inter-grain transport which proceeds through electron tunneling across barriers. At low temperatures the tunneling is suppressed giving rise to an insulating upturn in resistivity. While the effects of granularity are already evident at this level, the most surprising effects are revealed by magnetoresistance measurements.

A strong manifestation of the topological properties of surface states obeying the Dirac equation is the Berry phase of π associated with them [15, 20]. This is a consequence of the helical spin structure of the electrons in momentum space. Such an electron traversing a path which encircles the origin in momentum space, accumulates a phase of π upon completing the loop. This leads to a suppression of coherent back-scattering (Fig. 3 (a)). By applying a magnetic field, time reversal symmetry is broken and WAL can be destroyed giving rise to a negative magnetoconductance. All our samples indicate a sharp dip in the conductance with increasing magnetic field, indicating WAL (Figs. 3 (b-f)). For magnetic fields perpendicular to the sample, the magnitude of the dip increases with increasing thickness in the thin limit, but almost saturates for the thicker films (Fig. 3 (d)). In-plane field measurements however yield a surprisingly large magnetoresistance which is a consequence of predominant surface state transport as discussed later. We perform separate analysis for perpendicular field and parallel field magnetoconductance data (see Supplementary Information for details). The perpendicular field magnetoconductance data are fitted to the Hikami-Larkin-Nagaoka (HLN) equation that quantifies the conductance correction due to

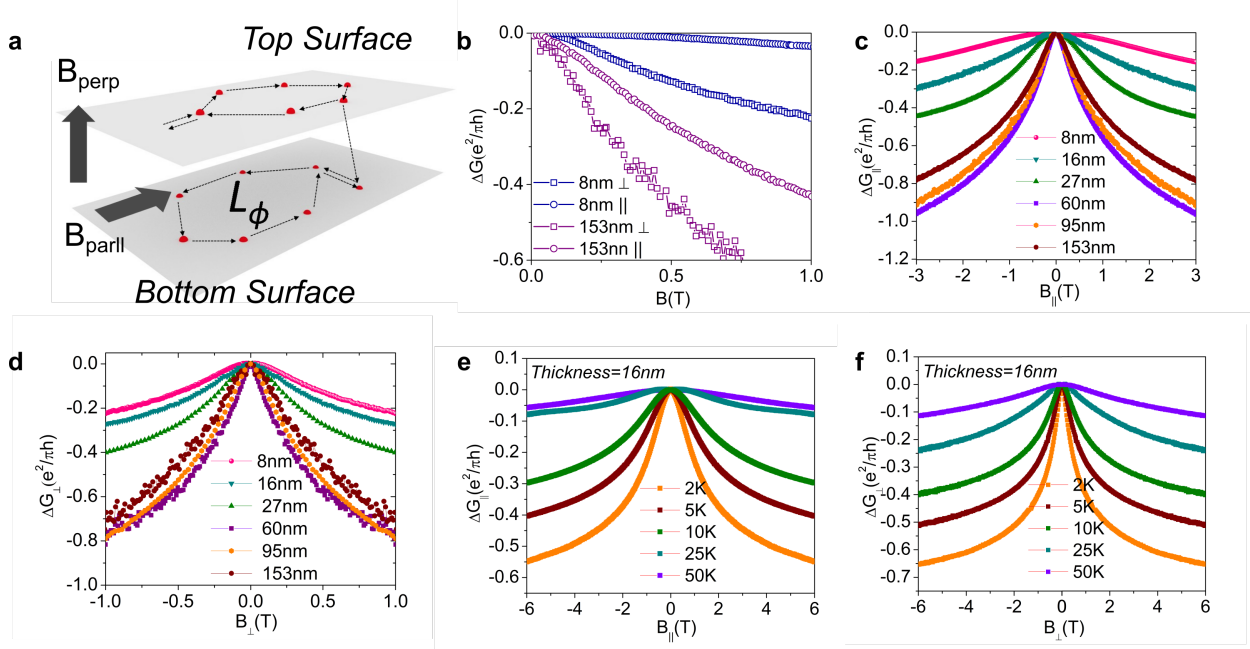


FIG. 3. **Weak Anti-localization correction to conductance** (a) Mechanism of WAL due to suppressed back-scattering. (b) Low-field magnetoconductance for $t = 8$ nm and $t = 153$ nm films for in-plane and out-of-plane field configurations. The magnetoconductance increases with thickness. Also, the low-field in-plane magnetoconductance is smaller in magnitude than the out-of-plane magnetoconductance. Thickness dependence of magnetoconductance for (c) parallel and (d) perpendicular fields. Temperature dependence of high-field magnetoconductance for (e) parallel and (f) perpendicular fields for a $t = 16$ nm film.

WAL in two dimensions [29–31],

$$\Delta\sigma_{\perp}(B_{\perp}) = \alpha_{\perp} \frac{e^2}{2\pi^2\hbar} \left[\psi \left(\frac{1}{2} + \frac{\hbar}{4el_{\phi}^2 B_{\perp}} \right) - \ln \left(\frac{\hbar}{4el_{\phi}^2 B_{\perp}} \right) \right] \quad (1)$$

in the limit of strong spin-orbit scattering, where σ is the sample conductivity, B_{\perp} is the applied magnetic field, l_{ϕ} is the phase coherence length, and $\psi(x)$ denotes the digamma function. While the perpendicular field magnetotransport gives information about the number of phase coherent channels and the associated decoherence lengths, the parallel field magnetotransport is a powerful tool for studying the spatial extent of the channels. In conventional TIs, the surface state penetration depth is small and therefore a parallel magnetic field does not decohere these channels. The only conductance correction therefore comes from the bulk of the sample. The complicated coupling between bulk and surface transport has however

made previous experimental findings ambiguous, and it has been pointed out that the parallel and perpendicular field magnetotransport cannot be consistently explained [32]. On the contrary, we find that conductance corrections arising out of bulk electrons in our samples are negligible, and clean signatures of surface state transport are obtained even in parallel field magnetoresistance measurements. We fit our parallel field data to the corresponding WAL equation for in-plane fields [33],

$$\Delta\sigma_{\parallel}(B_{\parallel}) = \alpha_{\parallel} \frac{e^2}{2\pi^2\hbar} \ln(1 + B_{\parallel}^2/B_{\phi}^2), \quad (2)$$

where $B_{\phi} = \hbar/(e\lambda l_{\phi})$, λ being the surface state penetration depth. In fitting our data, we take α_{\parallel} and λ as fitting parameters while the phase coherence length l_{ϕ} is used from the perpendicular field data. We assume that the phase coherence length for the two measurements must be same, if the contributions to conductance corrections come from the same channels in both cases.

The result of our analysis is shown in Fig. 4. In the thick-film regime (Fig. 4 (b)), $\alpha_{\perp/\parallel} \simeq 1$ for all ranges of temperature. More strikingly, the match between α_{\perp} and α_{\parallel} suggests that in both field configurations, the same channels contribute to WAL. Additionally $\alpha_{\perp/\parallel} \simeq 1$ indicates that both parallel and perpendicular magnetic fields interact with two distinct transport channels indicating a pair of decoupled topological surface states at the top and bottom of the film. In the thin film regime, perpendicular and in-plane field measurements again give the same values of α , but with $\alpha_{\perp/\parallel} \simeq 0.5$, indicating a coupling of the two surface states. Measurements over an entire thickness range indicate that this cross-over happens at around $t \approx 60$ nm (Figs. 4 (c-d)). Such clear signatures of coupling-decoupling transitions, for both in-plane and out-of-plane field configurations, have not been observed before for single TI thin films. Most transport studies on single TI films indicate a strong coupling between opposite surfaces even for thick films where direct tunneling due to overlap of surface state wave functions is not possible. Additionally, no signatures of the surface state transport have been observed in in-plane field magnetotransport. Our samples on the other hand show strong indications of surface state dominated transport, in both in-plane and out-of-plane measurement configurations.

The decoupling transition observed at $t \approx 60$ nm cannot be explained by existing ideas about TIs. We now show that the decoupling at such a large thickness is a consequence of the large penetration depth of surface states. As discussed before, the in-plane field

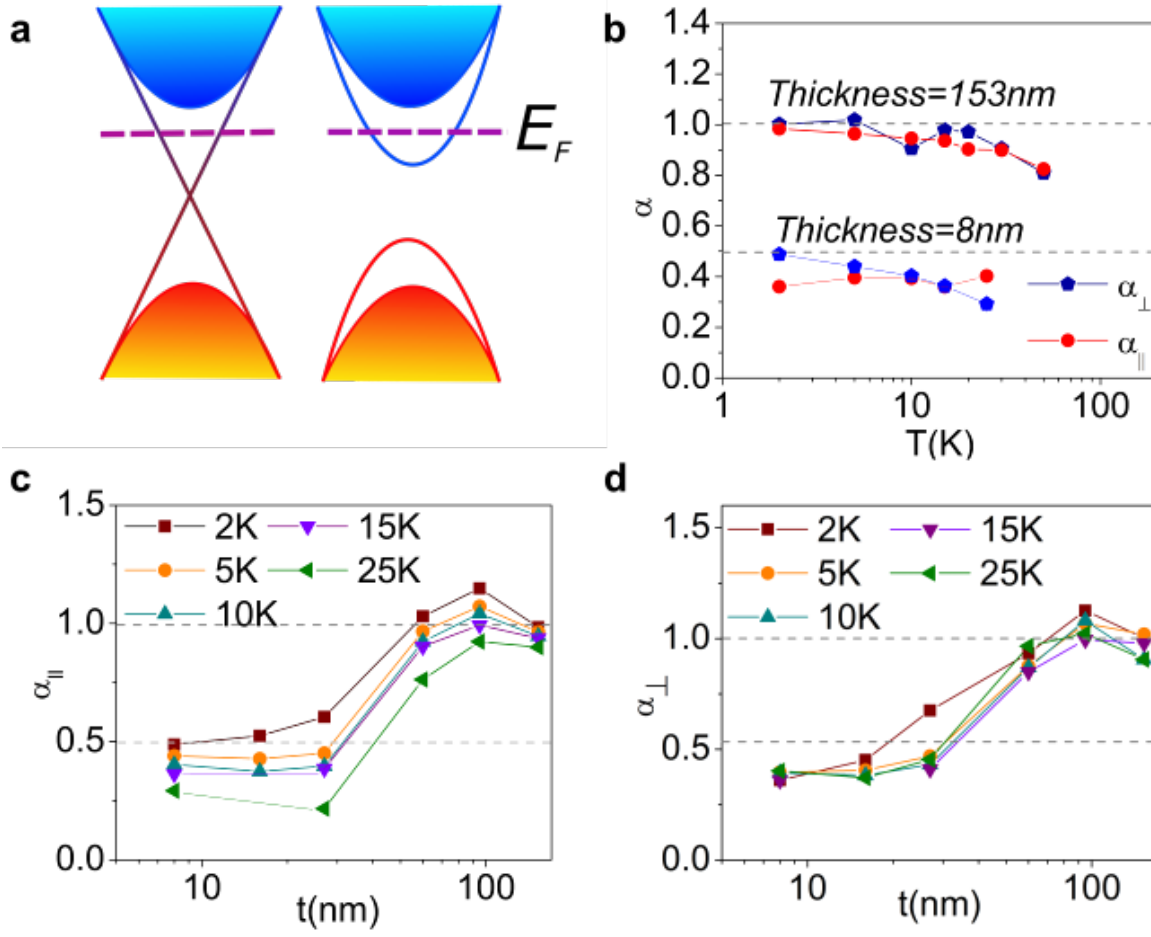


FIG. 4. **Transition from coupled to decoupled surface states** (a) Coupling of surface states causes hybridization between the two surface states and opens up a gap at the Dirac point. (b) α is shown as a function of temperature for 153 nm film in the decoupled regime and 8 nm film in the coupled regime. Both out-of-plane and in-plane field measurements give similar values of α within experimental accuracy. As a function of increasing thickness, (c) α_{\parallel} and (d) α_{\perp} undergo a cross-over from 0.5 indicating coupled surface states to 1.0 indicating decoupled surface states, with a decoupling transition at $t \simeq 60$ nm.

magnetoresistance depends critically on the cross-section of the states with which it interacts. For surface states, this cross-section is proportional to the surface state penetration depth for thick films. In the thin film limit, where surface states exist throughout the volume of the film, the cross-section is proportional to the thickness of the film. Fig. 5 (a) shows the extracted parameter λ which measures the extent of surface states in the z -direction.

In the thick film limit and low temperature, $\lambda \approx 33$ nm. This is approximately half the sample thickness for which we observe a decoupling transition. This is expected: the coupling transition commences when the thickness of the film is such that the top and bottom surface states extend throughout the bulk of the sample. This large penetration depth allows the surface states to interact even with a parallel magnetic field and give an unexpectedly large parallel field magnetoresistance. This allows us not only to accurately predict the surface state penetration depths, but also study their temperature dependence. The temperature dependence of λ shows a remarkable decrease with temperature for the thick films. On the other hand, for our thin samples λ is almost equal to the sample thickness and is very weakly dependent on temperature, most prominently observed for the thinnest measured film at $t = 8$ nm. The unusually large penetration depths and their temperature dependence is a consequence of the granularity as described below.

We can understand the various experimental results using a simple model of a granular TI (see Supplementary Information for details). Guided by the experimental observations that the grains are quite well-ordered and that the in-plane grain size is much larger than the perpendicular thickness, we consider a film consisting of a regular array of grains which are infinitely large in-plane (called the $x - y$ surface) and repeat periodically in the z -direction (along the c -axis) with a unit cell size $L \sim 2$ nm. We introduce intra-grain couplings t_1 and inter-grain couplings t_2 . (t_1 will depend strongly on the individual grain sizes; increasing the size of a grain increases the distance between its opposite surfaces and therefore decreases t_1). We consider surface states with a momentum $\vec{k} = (k_x, k_y)$. If the number of grains $N \gg 1$ (a thick film), we can introduce a Bloch momentum k_z in the z -direction (lying in the range $[-\pi/L, \pi/L]$). We then find a continuum of states with $E_{\vec{k},\pm} = \pm \sqrt{\hbar^2 v_F^2 \vec{k}^2 + t_1^2 + t_2^2 + 2t_1 t_2 \cos(k_z L)}$; this has a gap given by $2|t_1 - t_2|$. (Here v_F is the Fermi velocity on the $x - y$ surface and is given by 0.333 eV-nm/ \hbar for Bi₂Se₃ [12]). These form the bulk states of the film.

Next, if $t_1 < t_2$, we find states which are localized near the top and bottom surfaces of the film; these have the dispersion $E_{\vec{k},\pm} = \pm \hbar v_F |\vec{k}|$ and their wave functions decay into the bulk of the film with a penetration depth λ given by $e^{-L/\lambda} = t_1/t_2$. These are the surface states of the film (Fig. 5 (c)). There are no such states if $t_2 < t_1$. Thus the entire film behaves like a single TI with gapped bulk states and gapless surface states, and there is a quantum phase transition from a non-topological phase at $t_2 < t_1$ to a topological phase at

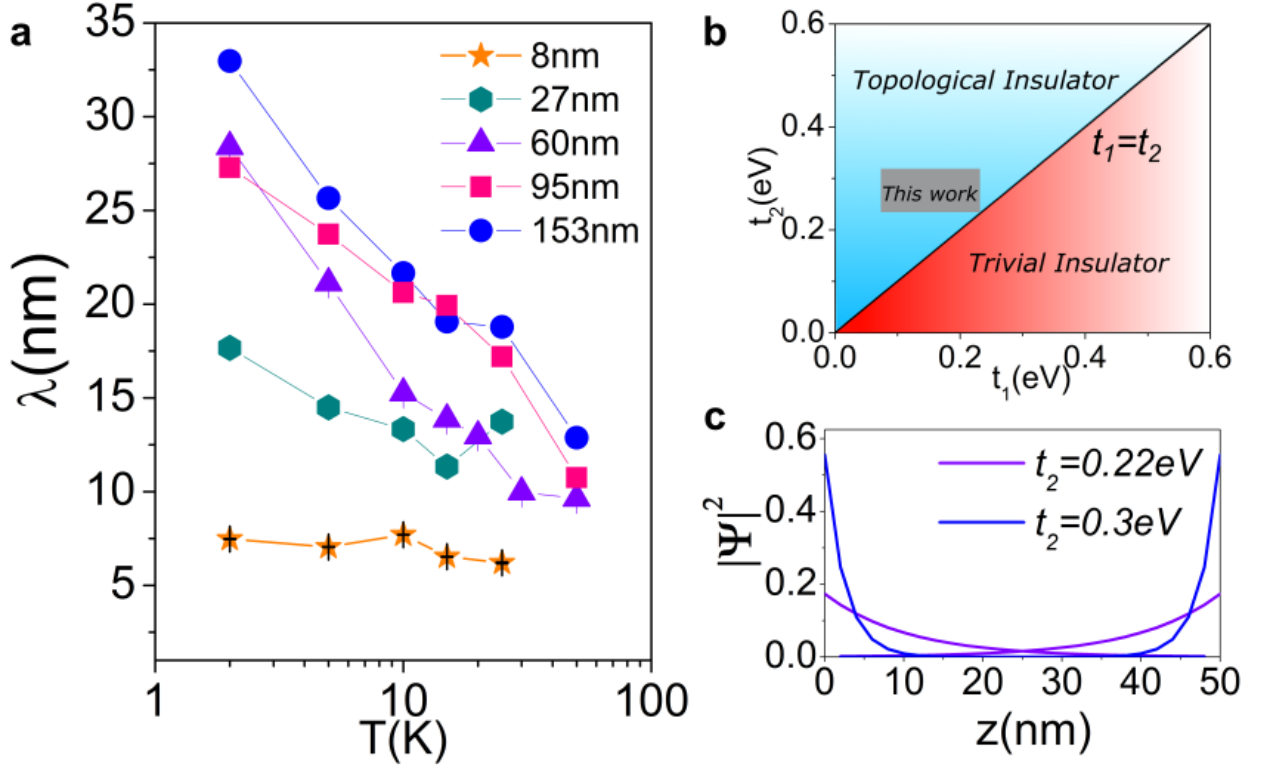


FIG. 5. **Surface state penetration depth in the TI regime** (a) Surface state penetration depth λ for different sample thicknesses and temperatures. For samples in the thick-film limit, λ decreases with increasing temperature from ~ 30 nm to ~ 15 nm. For thin samples, the temperature dependence of λ is weak and approaches the sample thickness. This allows us to estimate the ratio of intra-grain coupling (t_1) to inter-grain coupling (t_2). (b) shows that the interplay between t_1 and t_2 can give rise to a trivial insulator phase when $t_1 > t_2$ and topological insulator phase when $t_2 > t_1$. Our samples lie in the gray shaded area of this phase diagram. The ratio of t_1 to t_2 drastically modifies the surface state penetration depth. (c) shows the penetration of the z -component of top and bottom surface state wave functions into the bulk of the TI for two different values of t_2 at a constant value of $t_1 = 0.2$ eV.

$t_1 < t_2$. We now note that since the inter-grain coupling t_2 arises due to tunneling through a barrier given by the charging energies of two grains, it increases with the temperature in an activated form. On the other hand, the intra-grain coupling t_1 does not change the charging energy and is not expected to vary significantly with the temperature. Hence we expect t_1/t_2 and therefore λ to decrease with increasing temperature which agrees with our

observations. We observe from Fig. 5 (a) that for the thickest film, λ varies from about 33 nm at 2 K to 12 nm at 50 K. Taking the vertical grain size to be about 2 nm, the expression $e^{-L/\lambda} = t_1/t_2$ implies that t_1/t_2 varies from 0.85 to 0.94; hence the change with temperature is not large.

Finally, if $t_1 < t_2$ and the number of grains N is not very large, then there will be a significant hybridization between the states at the top and bottom surfaces. One can show that this is given by $\gamma \sim (t_1/t_2)^N$; the surface states then have the dispersion $E_{\vec{k},\pm} = \pm \sqrt{\hbar^2 v_F^2 \vec{k}^2 + \gamma^2}$ which has a gap $2|\gamma|$. We see that γ decreases both with increasing temperature (since t_2 increases) and increasing film thickness (since N increases).

In contrast, the surface states in conventional TIs are confined within ~ 2 -3 nm of the sample surfaces. The novelty of our TI is exemplified by the fact that the ratio of inter-grain to intra-grain tunneling determines the surface state penetration depth. When the two coupling strengths are nearly equal, the system is close to a topological phase transition and exhibits large surface state decay lengths. On increasing the temperature, the inter-grain coupling becomes stronger; this gives rise to a smaller penetration depth as we showed above. For thinner films, the top and bottom surface states are strongly coupled and span the entire bulk of the film; λ is then about the same as the film thickness. The response to temperature is weak in this limit. This counter-intuitive observation suggests that increasing the temperature makes the system become more ‘topological’. While we show that temperature can be used as a control for ‘topology’ in our system, it suggests that an ability to vary the ratio of the inter-grain coupling to the intra-grain coupling can be used to tune the various system parameters.

We now show how granularity can be used to vary the Berry phase. This phase can get modified from the ideal value of π for two reasons. First, the tunneling γ between the surface states effectively adds a mass term to the Dirac Hamiltonian describing those states; this modifies the Berry phase. The mass term also destroys ideal spin-momentum locking and effectively weakens the effect of the spin-orbit field B_{SOC} that quantifies this locking. While ARPES and STM measurements indicate a loss of spin-momentum locking for ultra-thin films [34, 35], a quantification of this loss has been missing in earlier work. Secondly, the application of a magnetic field that is comparable in strength to B_{SOC} causes the spins to get aligned in the direction of the magnetic field; this also modifies the Berry phase from π . Combining the effects of tunneling γ between the top and bottom surface states and a

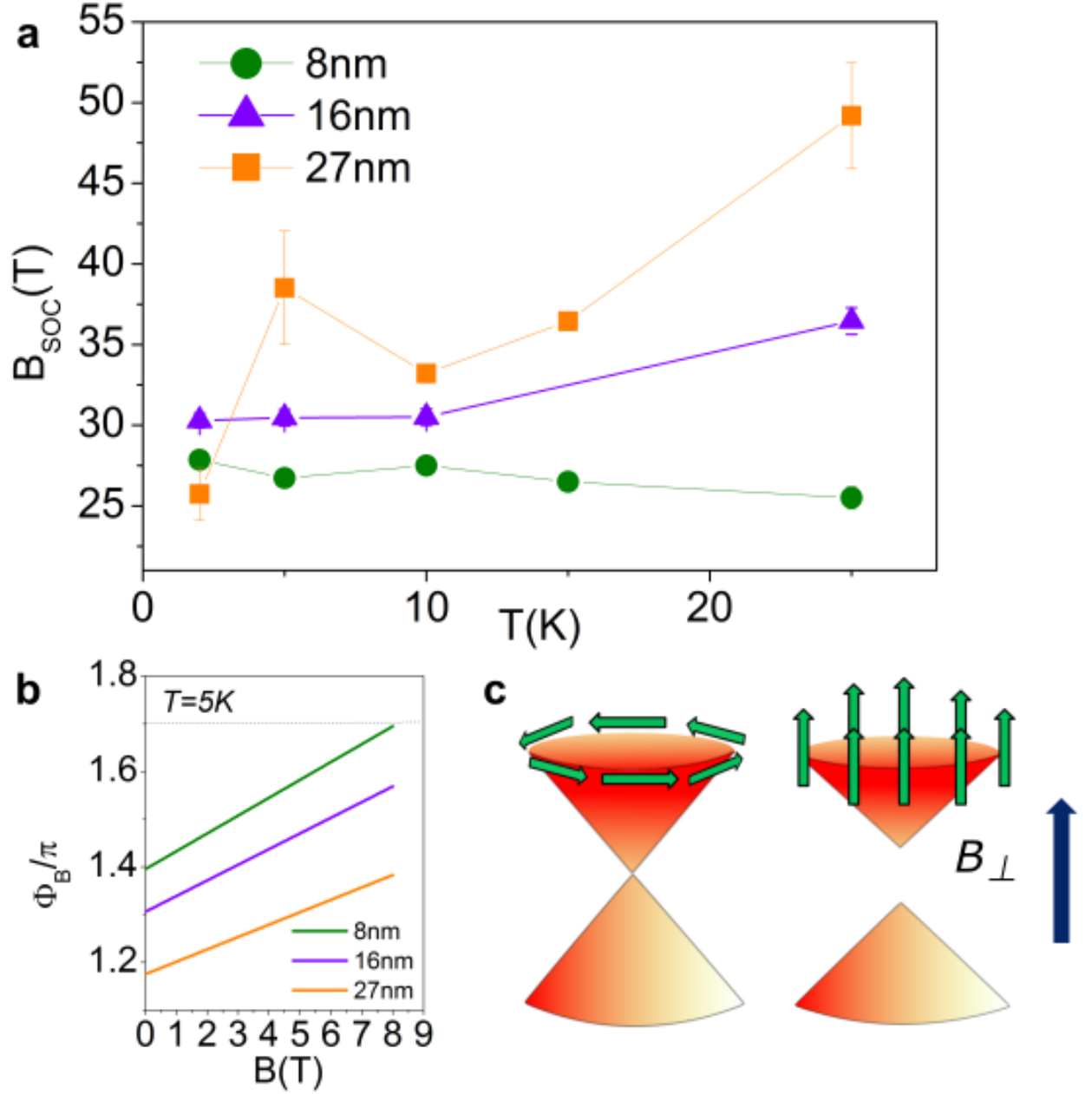


FIG. 6. **Berry phase effects** (a) Effective spin-orbit field as a function of temperature in the low-thickness limit. (b) Extracted dependence of the surface state Berry phase on magnetic field and sample thickness at $T=5K$. We chose only one state with all signs positive in Eq. (3). (c) Schematic showing how an external magnetic field B_{\perp} can compete with the intrinsic spin-orbit field to destroy the chiral spin momentum locking and give rise to a trivial Berry phase.

Zeeman magnetic field B_{\perp} applied in the z -direction, we find that there are four states Ψ_j

for a given momentum k_F . The Berry phases in these states are given by

$$\Phi_j = \pi \left(1 \pm \frac{b_z \pm \gamma}{\sqrt{\hbar^2 v_F^2 k_F^2 + (b_z \pm \gamma)^2}} \right), \quad (3)$$

where $b_z = g\mu_B B_\perp/2$ (g and μ_B are the gyromagnetic ratio and Bohr magneton respectively). Experimentally, this manifests as a sharp degradation of WAL at higher fields. The standard HLN equation can be used to fit the experimental data at small fields; however for large fields a large deviation is seen between the HLN equation and our data, with the HLN equation predicting a higher magnetoconductance than is observed. This strong suppression of WAL observed in the thin film limit can be explained by introducing a correction to the HLN equation which depends on the effective spin-orbit field B_{SOC} . Similar to prior works that have quantified the effect of Berry phase on WAL [36, 37], we use a phenomenologically modified HLN equation (see Supplementary Information for details) to capture this effect:

$$\begin{aligned} \Delta\sigma_\perp(B_\perp) = \alpha_\perp [1 - 2(B_\perp/B_{SOC})^2] \frac{e^2}{2\pi^2\hbar} \\ \times \left[\psi \left(\frac{1}{2} + \frac{\hbar}{4el_\phi^2 B_\perp} \right) - \ln \left(\frac{\hbar}{4el_\phi^2 B_\perp} \right) \right]. \end{aligned} \quad (4)$$

This allows us to extract the effective spin-orbit field B_{SOC} (Fig. 6 (a)). We find a strong thickness dependence of B_{SOC} with a value as small as ~ 30 T for $t = 8$ nm at 2 K. Further, we observe that this increases rapidly with increasing temperature and thickness. This can be explained as follows. The Fermi energy of our system is fixed by the Fermi level which is pinned to the conduction band bottom of the bulk states which come from the individual TI grains. The increase in mass of the Dirac fermions with decreasing thickness leads to an upward movement of the massive Dirac bands with the Fermi energy kept fixed. This gives rise to a decrease in the value of the surface k_F and a corresponding decrease in $B_{SOC} \propto v_F k_F$, accordingly modifying the Berry phase (Fig. 6 (b)). Such a competition of the Zeeman field with the internal spin-orbit field is difficult to observe in single crystal TIs because intrinsic SOC fields are of the order of several hundred Teslas. Introducing granularity decreases the effective spin-orbit field, and makes the study of interesting Dirac fermion physics experimentally feasible.

Granularity opens up an altogether different route to control the properties of TIs. We show that a multiply connected system composed of individual TI grains can, under certain conditions, behave as a single crystal TI but with spectacularly different properties.

Our granular thin films show distinct signatures of top and bottom surface states that are decoupled for thick films and get coupled below a critical film thickness. In stark contrast to single crystal TIs, these surface states exhibit a large penetration depth determined by grain size and inter-grain coupling and can be tuned by temperature; remarkably, the penetration depth is much larger than the thickness of a single grain. The Dirac nature of these states is clearly observed by studying the modification of their associated Berry phase in the presence of an external Zeeman field and tunneling between surface states, allowing a quantification of the intrinsic spin-orbit field. Future experimental and theoretical work can focus on careful tuning of the ratio of intra-grain coupling to inter-grain coupling that can drive such a system from a non-TI to a TI phase, allowing access to exotic topological phase transitions. Granularity may also be used to study topological Anderson insulators that are yet to be experimentally realized. Finally, the manipulation of spin transport in designer TIs may prove very interesting for the spintronics community.

Methods

Thin film growth: Thin films of Bi_2Se_3 were grown using pulsed laser deposition. The Bi-Se target was prepared by heating Bi (99.999%) and Se (99.999%) at 1123 K for 24 hours followed by slow cooling. Target composition was adjusted to compensate for Se loss during ablation. High resistivity (10 $\Omega\text{-cm}$) Si(111) substrates were used for deposition at a substrate temperature of ~ 523 K. The thin films were characterized using XRD, AFM, STM and Auger electron spectroscopy. We adjust the film growth rate by tuning the laser pulse energy, which also changes the morphology of the film from highly crystalline at low deposition rates to highly granular at high deposition rates. Granular films are grown at a high growth rate of ~ 60 pulses/nm. The thickness of the films is modified by changing the number of pulses fired, and verified using AFM measurements.

Transport measurements: Electrical transport measurements were carried out on six-probe Hall bars. The Hall bars were prepared by shadow deposition using metallic masks to prevent any contamination of the film from lithographic processing. Contacts were made using Silver paste. Measurements were carried out in a Oxford 2K Helium cryostat with a base temperature of 1.6 K and equipped with a 8 T superconducting magnet. Standard

low frequency AC Lock-in technique was used for resistance measurements. Sample bias currents were in the range of 100 nA to 1 μ A to avoid sample heating or high bias effects. The devices were aligned in different field configurations using specially designed sample holders for accurate sample placement. During in-plane magnetic field measurements, the samples were aligned such that the current direction was perpendicular to the direction of the in-plane magnetic field.

-
- [1] Beloborodov, I., Lopatin, A., Vinokur, V. & Efetov, K. Granular electronic systems. *Rev. Mod. Phys.* **79**, 469-518 (2007).
 - [2] Xu, K., Qin, L. & Heath, J. The crossover from two dimensions to one dimension in granular electronic materials. *Nature Nanotech.* **4**, 368-372 (2009).
 - [3] Fan, H. et al. Self-Assembly of Ordered, Robust, Three-Dimensional Gold Nanocrystal/Silica Arrays. *Science* **304**, 567-571 (2004).
 - [4] Chen, T. et al. Metal-insulator transition in films of doped semiconductor nanocrystals. *Nature Mater.* **15**, 299-303 (2015).
 - [5] Collier, C. et al. Reversible Tuning of Silver Quantum Dot Monolayers Through the Metal-Insulator Transition. *Science* **277**, 1978-1981 (1997).
 - [6] Chakravarty, S., Ingold, G., Kivelson, S. & Luther, A. Onset of Global Phase Coherence in Josephson-Junction Arrays: A Dissipative Phase Transition. *Phys. Rev. Lett.* **56**, 2303-2306 (1986).
 - [7] Sun, S. et al. Monodisperse FePt Nanoparticles and Ferromagnetic FePt Nanocrystal Superlattices. *Science* **287**, 1989-1992 (2000).
 - [8] Gur, I. et al. Air-Stable All-Inorganic Nanocrystal Solar Cells Processed from Solution. *Science* **310**, 462-465 (2005).
 - [9] Shirasaki, Y., Supran, G., Bawendi, M. & Bulovic, V. Emergence of colloidal quantum-dot light-emitting technologies. *Nature Photon.* **7**, 13-23 (2012).
 - [10] Kim, D., Lai, Y., Diroll, B., Murray, C. & Kagan, C. Flexible and low-voltage integrated circuits constructed from high-performance nanocrystal transistors. *Nature Commun.* **3**, 1216 (2012).
 - [11] Hasan, M. & Kane, C. Colloquium: Topological insulators. *Rev. Mod. Phys.* **82**, 3045-3067

- (2010).
- [12] Qi, X. & Zhang, S. Topological insulators and superconductors. *Rev. Mod. Phys.* **83**, 1057-1110 (2011).
 - [13] Chen, Y. et al. Experimental Realization of a Three-Dimensional Topological Insulator, Bi_2Te_3 . *Science* **325**, 178-181 (2009).
 - [14] Zhang, T. et al. Experimental Demonstration of Topological Surface States Protected by Time-Reversal Symmetry. *Phys. Rev. Lett.* **103**, 266803 (2009).
 - [15] Xia, Y. et al. Observation of a large-gap topological-insulator class with a single Dirac cone on the surface. *Nature Phys.* **5**, 398-402 (2009).
 - [16] Hsieh, D. et al. A tunable topological insulator in the spin helical Dirac transport regime. *Nature* **460**, 1101-1105 (2009).
 - [17] Roushan, P. et al. Topological surface states protected from backscattering by chiral spin texture. *Nature* **460**, 1106-1109 (2009).
 - [18] Hsieh, D. et al. Observation of Unconventional Quantum Spin Textures in Topological Insulators. *Science* **323**, 919-922 (2009).
 - [19] Peng, H. et al. Aharonov-Bohm interference in topological insulator nanoribbons. *Nature Mater.* **9**, 225-229 (2010).
 - [20] Fu, L. & Kane, C. Topological insulators with inversion symmetry. *Phys. Rev. B* **76**, 045302 (2007).
 - [21] Fu, L., Kane, C. & Mele, E. Topological Insulators in Three Dimensions. *Phys. Rev. Lett.* **98**, 106803 (2007).
 - [22] Roy, R. Topological phases and the quantum spin Hall effect in three dimensions. *Phys. Rev. B* **79**, 195322 (2009).
 - [23] Teo, J., Fu, L. & Kane, C. Surface states and topological invariants in three-dimensional topological insulators: application to $\text{Bi}_{1-x}\text{Sb}_x$, *Phys. Rev. B* **78**, 045426 (2008).
 - [24] Qi, X., Hughes, T. & Zhang, S. Topological field theory of time-reversal invariant insulators. *Phys. Rev. B* **78**, 195424 (2008).
 - [25] Zhang, H. et al. Topological insulators in Bi_2Se_3 , Bi_2Te_3 and Sb_2Te_3 with a single Dirac cone on the surface. *Nature Phys.* **5**, 438-442 (2009).
 - [26] Liu, C. et al. Model Hamiltonian for topological insulators. *Phys. Rev. B* **82**, 045122 (2010).
 - [27] Soriano, D., Ortmann, F. & Roche, S. Three-Dimensional Models of Topological Insulators:

- Engineering of Dirac Cones and Robustness of the Spin Texture. *Phys. Rev. Lett.* **109**, 266805 (2012).
- [28] Hsu, Y., Fischer, M., Hughes, T., Park, K. & Kim, E. Effects of surface-bulk hybridization in three-dimensional topological metals. *Phys. Rev. B* **89**, 205438 (2014).
- [29] Hikami, S., Larkin, A. & Nagaoka, Y. Spin-Orbit Interaction and Magnetoresistance in the Two Dimensional Random System. *Progress of Theoretical Physics* **63**, 707-710 (1980).
- [30] Altshuler, B., Khmel'nitzkii, D., Larkin, A. & Lee, P. Magnetoresistance and Hall effect in a disordered two-dimensional electron gas. *Phys. Rev. B* **22**, 5142-5153 (1980).
- [31] Garate, I. & Glazman, L. Weak localization and antilocalization in topological insulator thin films with coherent bulk-surface coupling. *Phys. Rev. B* **86**, 035422 (2012).
- [32] Lin, C. et al. Parallel field magnetoresistance in topological insulator thin films. *Phys. Rev. B* **88**, 041307(R) (2013).
- [33] Tkachov, G. & Hankiewicz, E. Weak antilocalization in HgTe quantum wells and topological surface states: Massive versus massless Dirac fermions. *Phys. Rev. B* **84**, 035444 (2011).
- [34] He, K. et al. Crossover of the three-dimensional topological insulator Bi₂Se₃ to the two-dimensional limit. *Nature Phys.* **6**, 584-588 (2010).
- [35] Jiang, Y. et al. Landau Quantization and the Thickness Limit of Topological Insulator Thin Films of Sb₂Te₃. *Phys. Rev. Lett.* **108**, 016401 (2012).
- [36] Mühlbauer, M. et al. One-Dimensional Weak Antilocalization Due to the Berry Phase in HgTe Wires. *Phys. Rev. Lett.* **112**, 146803 (2014).
- [37] Lu, H., Shi, J. & Shen, S. Competition between Weak Localization and Antilocalization in Topological Surface States. *Phys. Rev. Lett.* **107**, 076801 (2011).

Acknowledgements

K.M. thanks CSIR, India for financial support. D.S. thanks DST, India for support under Grant No. SR/S2/JCB-44/2010. P.S.A.K. acknowledges Nanomission, DST, Govt. of India for support.